4 × 8 Patch Array-Fed FR4-Based Transmit Array Antennas for Affordable and Reliable 5G Beam Steering

YONGYEON KIM[1], (Student Member, IEEE), HOGYEOM KIM[2,3], (Student Member, IEEE), INSEOP YOON[1], (Student Member, IEEE), AND JUNGSUEK OH[2,3], (Senior Member, IEEE)

[1]Department of Electronic Engineering, Inha University, Incheon 22212, South Korea
[2]Institute of New Media and Communications, Seoul National University, Seoul 08826, South Korea
[3]Department of Electrical and Computer Engineering, Seoul National University, Seoul 08826, South Korea

Corresponding author: Jungsuek Oh (jungsuek@snu.ac.kr)

ABSTRACT This paper presents a novel method of designing affordable 28-GHz transmit array antennas utilizing FR4 substrates, which are low-cost but lossy. It is demonstrated that low insertion loss can be achieved by employing appropriate combinations of spatial filter unit cells, where each unit cell is selected to minimize the loss factors defined by lossy spatial filter modeling. The loss factor with inter-layer couplings was found to be more variable than that without inter-layer couplings, although inter-layer couplings have previously been utilized to increase the tunable range of the phase shift. Therefore, the number of metal layers in the low-pass spatial filter more affected by the inter-layer coupling is selected to be less than the number of metal layers used in the bandpass spatial filter for a given thickness in the proposed method. In addition, a novel transmits array in which some of the unit cells are sinusoidally arranged is described. This can achieve up to 1.6-dB gain enhancement at some steered angles compared with the conventional design. To simulate transmit arrays rapidly, an effective simple medium structure representing a transmit array is presented. Finally, the measured results confirm the effectiveness of the proposed design approaches for affordable transmit array antennas. Only a small difference of 0.8 dB between the simulated and measured results confirms the successful manipulation of the lossy characteristic of FR4.

INDEX TERMS 28 GHz, 5G, FR4 transmit array, lossy circuits, patch array antennas, spatial filters, transmit array antenna.

I. INTRODUCTION

Recently, researchers have been actively studying antenna solutions for new-type 5G equipment such as mmWave repeaters and bases stations [1], [2]–[7], and one of the recent 5G equipment receiving much attention from the industry is 5G outdoor customer premise equipment where a total of 64 (8 × 8) antenna elements is used and each antenna array has 32 (4 × 8) elements for 2 × 2 MIMO [8]. In such applications, there is a practical challenge to achieve higher than 20 dBi antenna gain due to 4 × 8 antenna elements. Transmit arrays can perform a significant role in 5G communication as they transform arbitrary electromagnetic (EM) wavefronts

The associate editor coordinating the review of this manuscript and approving it for publication was Kwok L. Chung.

into a desired form, achieving substantial gain or coverage enhancement. Advanced transmit array technology utilizing spatial filters have been paid considerable attention to be combined with conventional phased array systems [9], [10]. In these transmit arrays, miniaturized phase shifters can compensate the phase profiles of incident wavefronts to construct plane waves [11]. The advantages of employing such transmit arrays are particularly evident in low-profile wireless communication systems, where the antenna gain decreases rapidly due to the limited antenna height. However, there is a definite trade-off between gain and cost because the dielectric materials typically used to construct these transmit arrays are very expensive [12], [13]. It is obvious that the insertion loss of a transmit array is a function of the loss tangent of the dielectric medium. Although low-loss substrates are

advantageous for transmit array performance [11], [13]–[16], the utilization of these materials is limited due to the afore-mentioned cost issue. It is essential for practical applications such as cost-effective mmWave 5G systems. FR4 substrates are widely used in commercial because of easy fabrication and low material cost but such substrate is very lossy to be applied to large-scale mmWave components. It has been reported that an antenna with an EM band-gap (EBG) res-onator can achieve gain enhancement even if it is made of a lossy substrate [17]–[19]. In a previous study, the struc-ture of an EBG, including a metallic unit cell consisting of a two-layered structure on a FR4 substrate and a metallic ground plane with a dipole antenna pattern, was constructed. In this structure, the antenna radiates EM energy by leaking waves from the substrate for gain enhancement [20]. How-ever, the design methods for EBG structures face greater challenges at millimeter wave frequencies, where complex topologies must be realized for much smaller unit cells. In addition, this type of superstrate structure suffers from a gain enhancement limit as the size of the antenna aperture increases.

Recently, advanced frequency selective surface (FSS) techniques have provided approximations of the capaci-tance and inductance in equivalent circuits of thin unit cells [21], [22]. A capacitance model represents EM in-plane coupling between nearby unit cells, while the inductance is related to the substrate thickness or metallic grid. The req-uisite values of the capacitance and inductance for a specific resonant frequency can be obtained using the aforementioned FSS approximation; thus, accurate spatial filter responses can be realized, even for higher orders. This approximation method allows for investigation of the relationships among the parameters of the equivalent circuits, such as the induc-tance and capacitance, and design parameters such as the dielectric constant, periodicity, and separation between adja-cent unit cells.

This paper presents novel design techniques employing lossy spatial filter modeling that enable affordable fabrication of transmit arrays made of lossy FR4 substrates. The thinner the substrate, the more the electric fields are coupled into other layers near them. Thus, this type of lossy substrate is affected by the thin structure of the spatial filter. Unit cells of this substrate were chosen after several simulation runs to determine the size yielding low insertion loss, employing dis-parate spatial filter arrays and mixed-order filter arrays tech-niques [14], [23]. It is demonstrated herein that the proposed FR4-based transmit array can provide levels of beam shaping and gain enhancement similar to those of ideally lossless substrate-based designs. In addition, a novel transmit array design called a sinusoidally arranged transmit array (SATA) is presented, whose unit cells are sinusoidally arranged. The SATA is designed to achieve gain enhancement at some steered angle compared to the conventional design. The remainder of this paper is organized as follows. In Section II, unit cells with lossy spatial filter responses and the relation-ship between resistance and loss tangent in equivalent circuit
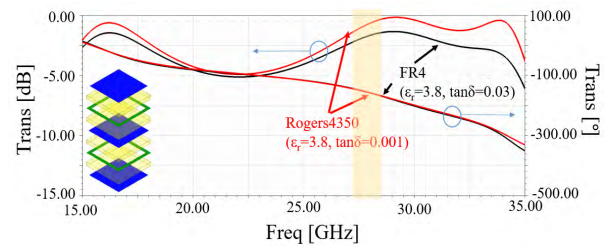

FIGURE 1. Frequency responses of bandpass unit cells on two different substrates: Rogers 4350 and FR4.

models of the unit cells are discussed. In this sense, the effects of the addition of resistance into the spatial filter model on the selection of the type of unit cells are discussed. In Section III-A, a 4 × 8 patch antenna array that is widely being considered for 5G outdoor customer premise equipment (CPE) is briefly introduced. In Section III-B, a novel structure called an effec-tive simple medium for transmit array simulation with high speed and that well represents FR4-based transmit arrays is presented.In Sections IV- A-C and V, the expected features of the transmit array structures are described, and full-wave EM simulations conducted using Ansys HFSS as well as the performances of the proposed fabricated transmit arrays are discussed based on measurements obtained with a reliable setup.

II. FR4-BASED TRANSMIT ARRAY USING LOSSY SPATIAL FILTER MODELING
A. LOSSY SPATIAL FILTER MODELING
This section describes the effects of the loss factors on the spatial filter response to enable the fabrication of an afford-able transmit array with a lossy substrate, FR4. Fig. 1 shows the frequency response of a bandpass unit cell consisting of five metallic layers on substrates with different loss tan-gents. The loss tangent of the substrate was chosen to be 0.03 for FR4 and 0.001 for Rogers 4350, while the dielectric constant was 3.8 in both cases. Each unit cell consisted of three metallic patches(blue) and two metallic grids(green). The lateral dimensions of the three metallic patches were 1.8 mm, 1.875 mm, and 1.825 mm, and the width each metallic grid was 0.1 mm. The red solid and black dashed lines in Fig. 1 indicate the insertion losses and phase shifts of the unit cells made of Rogers4350 and FR4, respectively. The insertion loss of the FR4 unit cell at 28 GHz is approx-imately 0.8 dB higher than that of the Rogers 4350 unit cell, while their phase shifts are almost the same. The con-ventional equivalent circuit of the bandpass unit cell cannot explain this discrepancy. To address this issue, a resistance representing the dielectric loss was added to the equivalent circuit of the metal layer. Figs. 2 and 3 depict the unit cells of low-pass and bandpass FSSs, respectively, together with their conventional and modified equivalent circuits. In the equivalent circuits, the inductance and capacitance induced by the metal layers are functions of the dielectric constant of the substrate. Another inductance generated by the dielectric
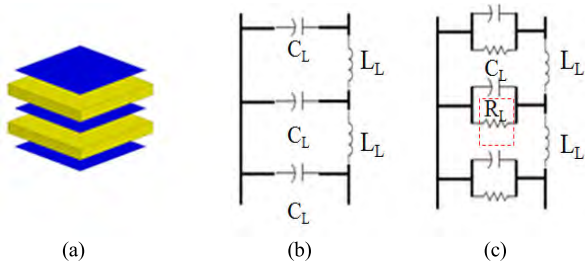
FIGURE 2. (a) Unit cell with a low-pass response, (b) conventional equivalent circuit of the low-pass unit cell, and (c) equivalent circuit including the loss factor.
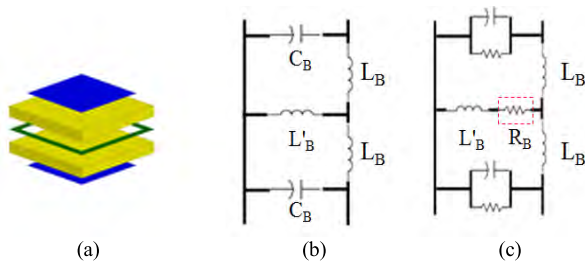
FIGURE 3. (a) Unit cell with a bandpass response, (b) conventional equivalent circuit of the bandpass unit cell, and (c) equivalent circuit including the loss factor.

substrate (L_L and L_B) is a function of the substrate thickness [21]. The resistances in the dashed red box in Fig. 2 (c) (denoted R_L) and Fig. 3 (c) (denoted R_B), correspond to the losses caused by the middle layer of the low-pass and bandpass FSS unit cells, respectively. Since the substrate is very thin compared to the lateral dimension of the unit cell, the losses related to L_L and L_B in the equivalent circuits are negligible. Fig. 4 presents a unit cell model for full-wave EM simulations that was used to acquire the resistance as a function of the loss tangent. Two floquet ports are located on the top and bottom planes. The incident waves propagate from the top plane to the bottom plane, as depicted in Fig. 4 (a) and (b). The dielectric media filling the volume between the two floquet ports were chosen to be FR4 and Rogers 4350. In the conventional low-loss FSS unit cell, while the equivalent series LC circuit of Fig. 4 (a) includes a series inductor as well as a series capacitor, the series inductor can be ignored by considering the shape of the patches having a wide lateral dimension dominantly exciting capacitive in-plane coupling [24]. Similarly, a shunt capacitor in the equivalent parallel LC circuit of Fig. 4 (b) can be ignored. Fig. 4 (c) and (d) show the aforementioned approximation [25]. Finally, considering the lossy characteristic of FR4, a resistance representing the loss factor can be added to the equivalent circuits of Fig. 4 (c) and (d). In-plane couplings across the gap between the metallic patches and the associated loss factor in Fig. 4 (a), correspond to the shunt capacitance and shunt resistance in Fig. 5 (a), respectively. Similarly, the stored magnetic energy induced along the metallic grid and the associated loss factor in Fig. 4 (b) correspond to the
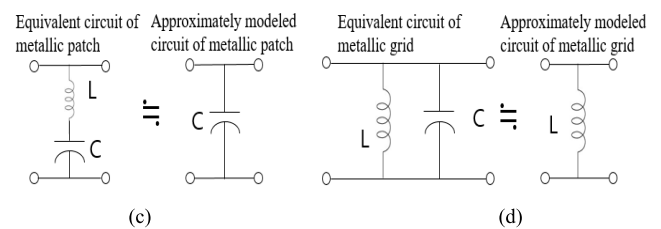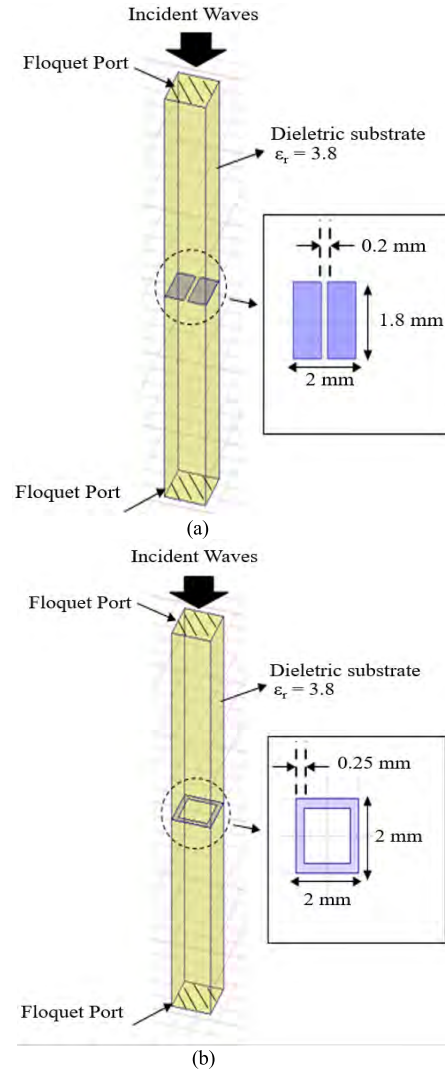
FIGURE 4. Full-wave EM simulation models of (a) a metallic patch and (b) a metallic grid, and equivalent circuits of (c) the metallic patch and (d) metallic grid.

series inductance and series resistance in Fig. 5 (b), respectively.

$$Z_{11,patch} = \frac{R_1}{1 + \omega^2 R_1^2 C_1^2} - j\frac{\omega R_1 C_1}{1 + \omega^2 R_1^2 C_1^2} \quad (1)$$

$$R_{patch} = \left[1 + \left(\frac{Im[Z_{11,patch}]}{Re[Z_{11,patch}]} \right)^2 \right] \times Re[Z_{11,patch}] \quad (2)$$
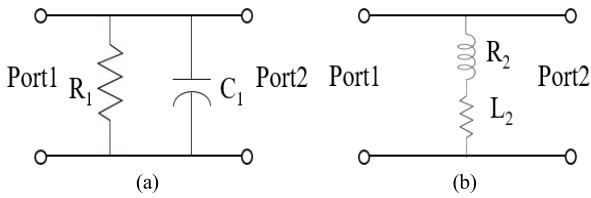
FIGURE 5. Lossy circuit models of (a) a metallic patch and (b) a metallic grid.

$$Z_{11,grid} = R_2 + j\omega L_2 \tag{3}$$
$$R_{grid} = Re[Z_{11,grid}] \tag{4}$$
$$Re[Z_{11,patch}] \cong 0.07(1 + 1000\tan\delta) \tag{5}$$
$$Re[Z_{11,grid}] \cong 0.45(1 + 15\tan\delta) \tag{6}$$

The resistance can be derived to be a function of the loss tangent in the following manner. First, Z_{11} is extracted from the full-wave EM simulation model shown in Fig. 4. Second, the impedance summation of the lumped elements in Fig. 5 is calculated and the total impedance must be equal to the Z_{11} value extracted using the full-wave EM simulation. Finally, the values of the reactive elements and the resistance can be acquired through the aforementioned comparison. If a metallic patch is employed, the sum of the impedances is given by (1). The patch resistance (R_{patch}) can be obtained by plugging the real and imaginary parts of (1) into (2). If a metallic grid is employed, the sum of the impedances is given by (3); thus, the grid resistance (R_{grid}) can be obtained from (4). Figs. 6 (a) and (b) and Figs. 7 (a) and (b) show the real and imaginary parts, respectively, of the Z_{11} parameters obtained from full-wave EM simulation of the metallic patch and grid. In addition, the approximate functions for the real parts of Z_{patch} and Z_{grid} are shown in (5) and (6), respectively. The average imaginary patch and grid values are -65.82 and 58.58, respectively. The patch resistance can be obtained by inputting (5) and an imaginary value into (2). Similarly, the grid resistance can be obtained by inputting (6) into (4). Therefore, the resistance represents the dielectric loss as a function of the loss tangent. Fig. 6 (a) shows that the real part of Z_{patch} varies between 0 and 3.5 when the loss tangent varies between 0 and 0.05, while in Fig. 6 (b) the real part of Z_{grid} only varies between 0.4 and 0.8 for the same loss tangent range. The rate of change of the real part of Z_{patch} with respect to the loss tangent is nearly 70, while the rate of change of the real part of Z_{grid} is as small as 6.75. Since loss tangent has no unit, the unit of the rate of the change is Ohm. Accordingly, this finding suggests that the magnitude and rate of variation are higher in the metallic patch case than in the metallic grid case. The electric fields of metallic grid layers are less coupled to other layers near them than those of patch layers. Therefore, unit cells utilizing metallic patches are more sensitive to loss tangent variations than unit cells employing metallic grids. Based on the aforementioned characteristics, spatial filter unit cells are addressed in the following section.
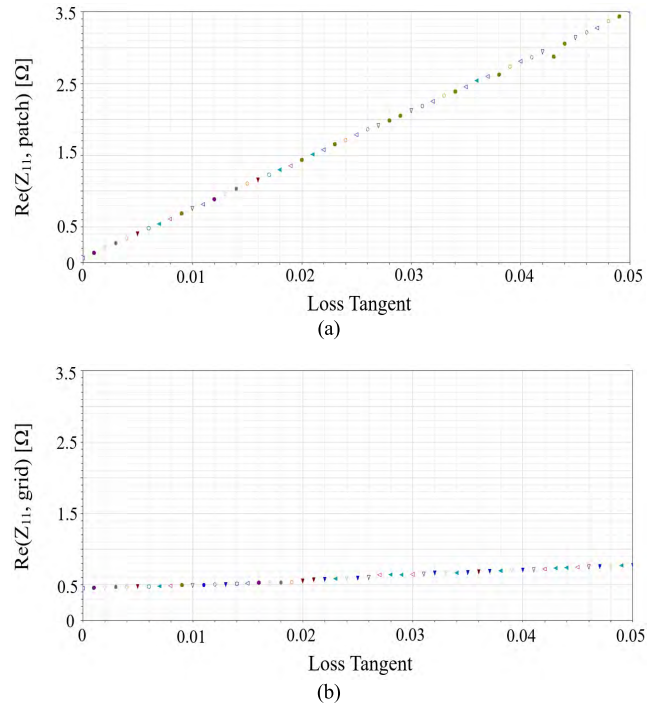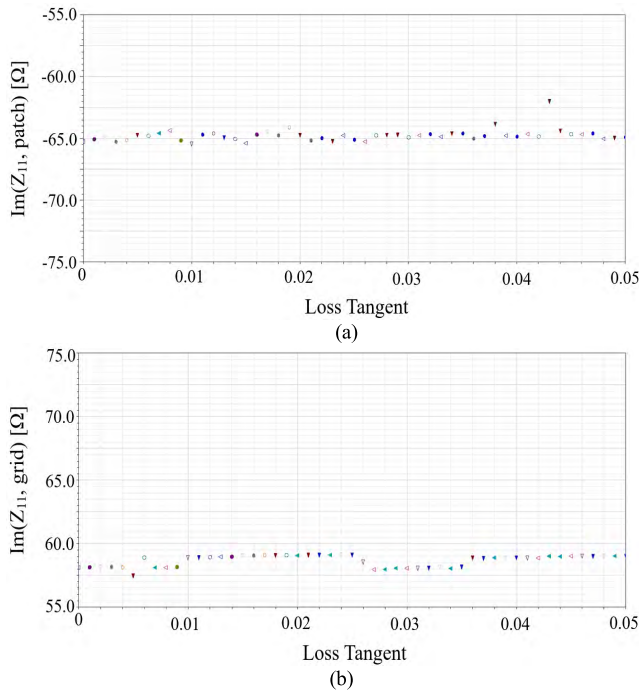

FIGURE 6. Real parts of (a) $Z_{11,patch}$ and (b) $Z_{11,grid}$ obtained from full-wave EM simulation of a unit metallic patch and grid.

### B. MIXED-ORDER COMBINATIONS OF DISPARATE LOSSY SPATIAL FILTERS

It is difficult to obtain a wide tunable range for the phase shift using a conventional transmit array design because uniform-order spatial filter arrays have typically been used. The common method of increasing the tunable range of the phase shift has been to increase the order of the spatial filters. Recently, transmit array design employing mixed-order spatial filters has been introduced to reduce fabrication costs by decreasing the number of metal layers [14]. In this method, at least two spatial filters having different-order responses are utilized, enabling affordable transmit array fabrication while maintaining a similar tunable range of the phase shift. Another approach is to design transmit arrays utilizing disparate spatial filter arrays [23]. In this method, multiple types of spatial filters are employed to achieve a wide tunable range of the phase shift. However, based on our analysis of the dielectric loss as a function of the loss tangent, the utilization of such approaches without considering the loss factor may substantially increase the dielectric loss and fabrication cost. In this study, four different types of unit cells created by mixed-order combinations of disparate lossy spatial filters were utilized. Fig. 8 shows the structures of the four unit cells: two low-pass spatial filters with different orders (third and fifth) [13], [22] and two bandpass spatial filters with different orders (second and third) [25].

Each structure contains four FR4 substrates but has a different number of metal layers. The dimension parameters of the metallic patches are denoted as P1, P2, and P3, and

FIGURE 7. (a) Imaginary parts of $Z_{11,patch}$ and (b) f $Z_{11,grid}$ obtained from full-wave EM simulation of a unit metallic patch and grid.
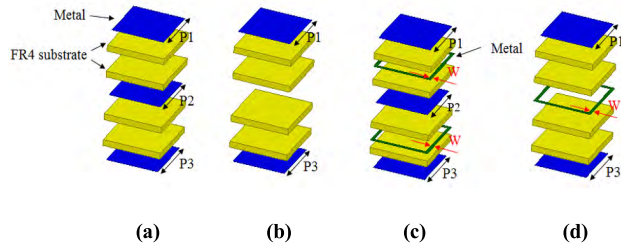

FIGURE 8. Exploded views of spatial filters with: (a) fifth-order low-pass response, (b) third-order low-pass response, (c) third-order bandpass response and (d) second-order bandpass response.

the width parameter of the metallic grids is denoted as W. If the unit cell consists of only patches (called an ''all-patch'' structure) some metal layers are truncated to minimize the losses, as shown in Figs. 8 (a) and (b). In contrast, the metal layers in the bandpass unit cell are not removed because the aforementioned all-patch structure is more sensitive to the loss factor than the bandpass unit cell consisting of both patches and grids. The widths of the metallic grids in Figs. 8(c) and (d) are designed to be the same. Fig. 9 shows the unit cell transmittance in dB as functions of the patch and grid sizes. The proposed unit cells maintain an insertion loss of less than 1.5 dB at 28 GHz. Fig. 10 shows the unit cell transmittance in degree as functions of the patch and grid sizes, demonstrating that the different types of spatial filters can cover different tunable ranges of the phase shift, leading to an increase in the total tunable range of the phase shift. The proposed unit cells cover an approximate tunable range of 190°, which is similar to the tunable range achieved in a
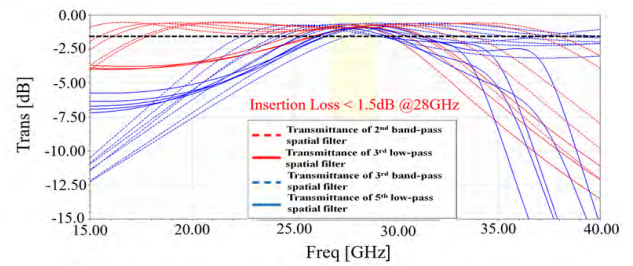
FIGURE 9. Transmittances (dB) of the third- and fifth-order low-pass and second- and third- order bandpass spatial filters as functions of the patch and grid sizes.
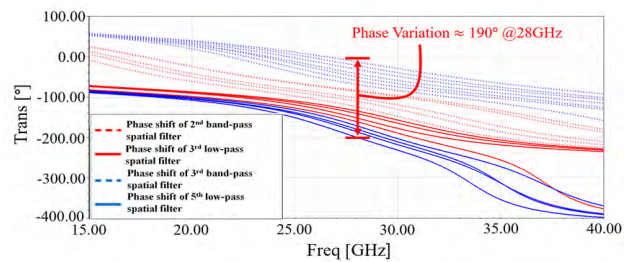
FIGURE 10. Transmittances (degree) of the third- and fifth-order low-pass and second- and third-order bandpass spatial filters as functions of the patch and grid sizes.

previous study using a low-loss substrate [14], Rogers 6010, whose loss tangent is very low (0.002). Table 1 lists the patch sizes, phase shifts, and insertion losses of the third- and fifth-order low-pass and second- and third- order bandpass spatial filters depicted in Figs. 9 and 10.

III. 4 × 8 PATCH ARRAY ANTENNA AND EFFECTIVE SIMPLE MEDIUM STRUCTURE
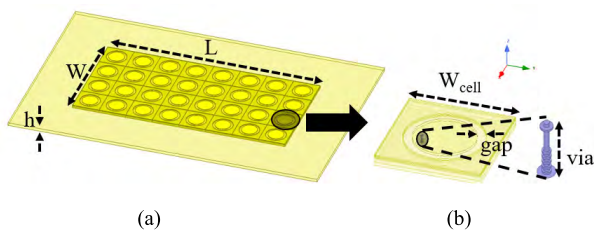
A. 4 × 8 PATCH ARRAY ANTENNA

As an initial study, a 4 × 8 patch array antenna, which is widely being considered for 5G repeaters and CPE, was chosen as the antenna source. The 4 × 8 patch array antenna operating at 28 GHz shown in Fig. 11 was designed using a 10-layer FR4 stacked substrate. Because of fabrication cost, FR4 is widely used in commercial mmWave 5G antenna-in-package solutions [1], [26]–[29]. Via wall is surrounded with copper for cavity structure. In Fig. 11, W, L, h, W_{cell}, gap and height of via were set to 22 mm, 44 mm, 0.609 mm, 5.5 mm, 0.5 mm, 0.444 mm. The simulated 10-dB return loss bandwidth is 1 GHz shown in Fig.12. The gain is 19.5 dBi at the target frequency of 28 GHz.

B. EFFECTIVE SIMPLE MEDIUM STRUCTURE

Since a transmit array comprised of FR4 unit cells takes a long time to simulate, a novel structure for transmit array simulation is presented in this paper: an effective simple medium structure that has no loss tangent. For the simulation, the unit cells of the FR4-based transmit array are replaced by an effective simple medium structure where the relative

TABLE 1. Patch size, grid size, phase shift, insertion loss for third- and fifth-order low-pass and second- and third- order bandpass spatial filters.

| UC #	Filter Type	Order	P1 (mm)	P2 (mm)	P3 (mm)	W (mm)	Phase (°)	IL (dB)
1	BP	3th	0.75	0.85	0.7	0.1	-12.89	1.34
2	BP	3th	0.85	0.9	0.825	0.1	-22.17	0.98
3	BP	3th	0.925	1	0.85	0.1	-31.50	0.68
4	BP	3th	1.025	1.1	0.875	0.1	-42.47	0.65
5	BP	3th	1.025	1.15	0.875	0.1	-50.08	0.79
6	BP	3th	1	1.275	0.95	0.1	-59.38	1.17
7	BP	3th	1.175	1.25	1.15	0.1	-68.89	1.29
8	BP	2rd	1.25	-	1.225	0.1	-83.73	0.98
9	BP	2rd	1.3	-	1.25	0.1	-86.11	0.95
10	BP	2rd	1.425	-	1.4	0.1	-102.56	0.89
11	BP	2rd	1.5	-	1.55	0.1	-110.82	0.85
12	BP	2rd	1.575	-	1.5	0.1	-124.33	0.70
13	LP	3rd	1.625	-	1.5	-	-134.57	0.89
14	LP	3rd	1.65	-	1.6	-	-141.10	0.92
15	LP	3rd	1.675	-	1.6	-	-151.95	0.74
16	LP	5th	1.625	1.65	1.5	-	-161.12	0.90
17	LP	5th	1.725	1.75	1.65	-	-171.28	0.98
18	LP	5th	1.675	1.8	1.5	-	-179.80	0.91
19	LP	5th	1.725	1.825	1.65	-	-186.06	1.04
20	LP	5th	1.625	1.825	1.75	-	-199.71	0.99

FIGURE 11. (a) Oblique view of the 4 × 8 patch array antenna, (b) patch cell and feeding structure.
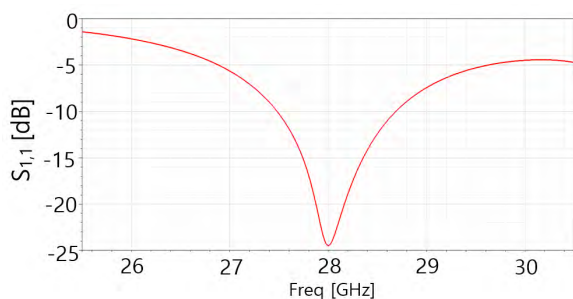
FIGURE 12. S$_{11}$ of the 4 × 8 patch array antenna at 28 GHz.

permittivity and permeability of the unit cells are changed to the same extent. This enables dramatic changes in the guided wavelength ($= \lambda_0 / \sqrt{\mu\varepsilon}$) related to the phase shift by the unit
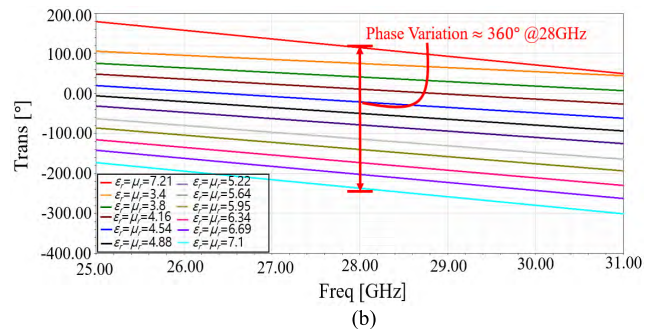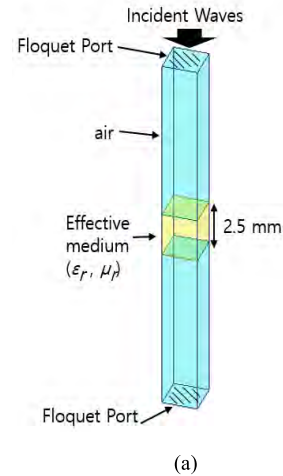
FIGURE 13. (a) Effective simple medium structure and (b) tunable range of the phase shift.

cells while the wave impedance ($= \sqrt{(\mu / \varepsilon)}$) is maintained at a constant value of 377 ohms which indicates the passband. The proposed effective simple medium structure technique results in high simulation speed and relatively accurate transmit array representation. Fig. 13 (a) shows an effective simple medium structure.

Two floquet ports are located on the top and bottom planes, and incident waves propagate from the top plane to the bottom plane. The effective simple medium structure is surrounded by air, and the height of the effective simple medium structure was chosen to be 2.5 mm. The unit cell size was selected to be 2 mm×2 mm, and ε_r and μ_r were determined according to the desired phase shift. Fig. 13 (b) shows the 360° tunable range of the phase shift, which can be achieved by changing the phase constant in the wave equation using the ε_r and μ_r values of the effective simple medium structure. Since the lateral dimension of the unit cell was selected to be 2 mm, a corresponding effective simple medium structure was determined every 2 mm from the center of the transmit array to compensate the required phase shift from Fig. 14. Fig. 15 shows a comparison of the radiation patterns of the effective medium-based array and the fabricated FR4-based transmit array. There is an error of 0.8 dB between effective medium and fabricated FR4-based transmit array.
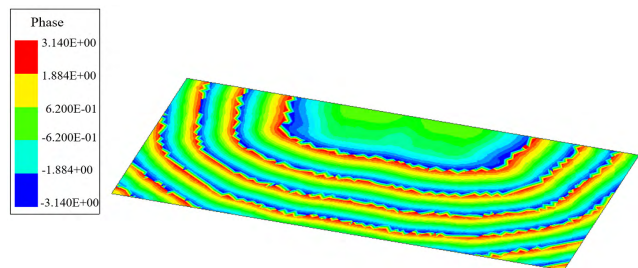
FIGURE 14. Phase profiles of E-fields radiated by the 4 × 8 patch array antenna at a target distance of 30 mm from the antenna array.
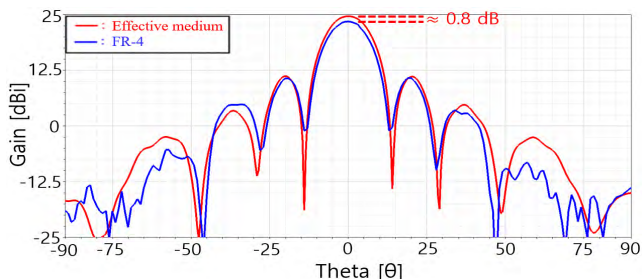

FIGURE 15. Comparison of the radiation patterns of the designed effective medium-based array and the fabricated FR4-based transmit array.

IV. MACRO DESIGN OF FR4-BASED TRANSMIT ARRAYS

A. MACRO DESIGN OF FR4-BASED E-TA

This section presents a macro design procedure for the FR4-based transmit array employing mixed-order and disparate lossy spatial filter arrays. Based on the discussions in Sections II-A and B, the proposed transmit array design steps are as follows.

Step 1. Select the type of antenna source, target distance between the transmit array aperture and antenna source, and aperture area, according to the system requirements. In this case, the aforementioned 4 × 8 patch array antenna was selected as the antenna source, the antenna size was 22 mm×42 mm, and the target distance was selected to be 30 mm. The transmit array was designed with a semi-major axis a = 92 mm and semi-minor axis b = 76 mm for axial ratio a/b = 1.2778.

Step 2. Capture the phase-front of the EM waves emitted by the antenna source over the selected aperture at the selected distance, by performing full-wave EM simulations. Fig. 14 shows these phase profiles on the half plane of the aperture. Since the lateral dimension of the unit cell was selected to be 2 mm, the phases were captured every 2 mm to obtain numerous observation points.

Step 3. Calculate the requisite phase shifts at all of the captured points to realize a uniformly flat wave-front, creating a plane wave for high gain.

Step 4. Based on the determined phase shifts in Section II-B, select the type of unit cell required for each point

TABLE 2. Distance from the center of the aperture along the x-axis, required phase shift, and selected unit cell number (UC#) for each distance for E-TA.

| #	Distance from the center of the aperture(mm)	Required phase (°)	UC #	#	Distance from the center of the aperture(mm)	Required phase (°)	UC #
1	0	-29.2013	3	21	40	-272.909	20
2	2	-29.2568	3	22	42	-218.456	20
3	4	-24.9446	2	23	44	-170.887	17
4	6	-17.7448	2	24	46	-110.26	11
5	8	-7.73013	1	25	48	-60.9873	6
6	10	-357.816	1	26	50	-6.10273	1
7	12	-346.597	1	27	52	-313.706	1
8	14	-338.311	1	28	54	-253.963	20
9	16	-333.083	1	29	56	-200.814	20
10	18	-329.667	1	30	58	-145.565	14
11	20	-318.398	1	31	60	-89.3696	9
12	22	-292.904	20	32	62	-29.2323	3
13	24	-263.395	20	33	64	-334.905	1
14	26	-232.838	20	34	66	-274.938	20
15	28	-188.997	19	35	68	-216.8	20
16	30	-154.189	15	36	70	-158.283	16
17	32	-107.542	10	37	72	-101.646	10
18	34	-63.2793	6	38	74	-36.4172	4
19	36	-15.0969	2	39	76	-338.551	1
20	38	-324.231	12	-	-	-	-

from Table 1. To obtain the widest tunable range of the phase shift from the combined topology of the numerous unit cells, determine the order and type of the FSS responses of the unit cells based on the discussions in Sections II-A and B. The required numbers of substrates and metal layers are also determined in this step.

For a target distance of 30 mm between the transmit array and the patch array antenna, Table 2 and 3 present the distances between the captured points and the center of the transmit array aperture and the required phase shift and selected unit cell number (denoted as UC#) for each distance. It should be noted that the unit cells in Table 2 and 3 correspond to half of the whole transmit array structure. These profiles are repeated in the other half of the structure, due to the symmetry of the transmit array structure. The tunable range of the phase shift in Table 1 can be utilized to design transmit arrays, but some of the required phase shifts in Table 2 and 3 are outside the tunable range of 190°. To compensate the phase shifts outside the tunable range, two types of unit cells were used. The UC1 representing a phase shift of −10° was, as an alternative, selected to cover the tunable range from −285° to −360°, and the UC20 representing the phase shift of −200° was, as an alternative, selected to cover the tunable range from −200° to −285°. For the transmit array simulation, unit cells of the FR4-based transmit array were replaced by an effective medium structure.

TABLE 3. Distance from the center of the aperture along the y-axis, required phase shift, and selected unit cell number (UC#) for each distance for E-TA.

| #	Distance from the center of the aperture(mm)	Required phase (°)	UC #	#	Distance from the center of the aperture(mm)	Required phase (°)	UC #
1	0	-29.2013	3	25	48	-220.123	20
2	2	-29.2613	3	26	50	-194.231	19
3	4	-30.1234	3	27	52	-156.187	15
4	6	-30.2231	3	28	54	-104.213	10
5	8	-31.4512	3	29	56	-57.125	6
6	10	-31.962	3	30	58	-23.868	2
7	12	-32.124	3	31	60	-122.124	12
8	14	-32.612	3	32	62	-269.612	20
9	16	-33.8123	3	33	64	-170.912	17
10	18	-34.8239	3	34	66	-118.612	11
11	20	-32.412	3	35	68	-110.347	11
12	22	-31.196	3	36	70	-62.964	6
13	24	-29.175	3	37	72	-300.612	1
14	26	-27.972	3	38	74	-240.645	20
15	28	-24.124	2	39	76	-149.523	14
16	30	-23.762	2	40	78	-97.242	9
17	32	-22.171	2	41	80	-34.624	3
18	34	-20.362	2	42	82	-300.215	1
19	36	-17.231	2	43	84	-240.682	20
20	38	-14.752	1	44	86	-169.476	16
21	40	-12.321	1	45	88	-106.23	10
22	42	-5.612	1	46	90	-47.893	4
23	44	-320.671	1	47	92	-330.231	1
24	46	-274.851	20	-	-	-	-
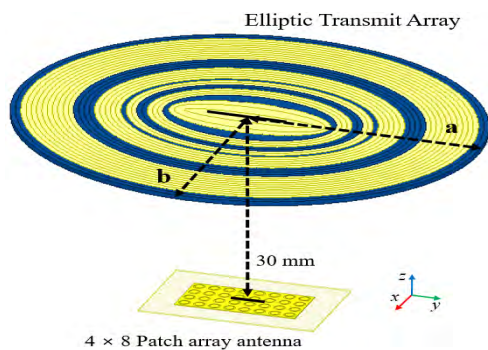
FIGURE 16. Oblique perspective of the proposed effective medium-based E-TA fed by a 4 × 8 patch array antenna.

Fig. 16 shows an oblique view of the proposed low-profile effective medium-based elliptic transmit array, denoted as E-TA fed by the 4 × 8 patch array antenna. The gain enhancement in YZ-plane of the proposed E-TA relative to that of the patch array antenna for POs of 0°, −45°, −90°, and −135° is observable in the full-wave EM simulation results in Fig. 17. The solid lines are the radiation patterns of the antenna with the proposed E-TA, and the dashed lines are the radiation patterns of the antenna without any transmit array.
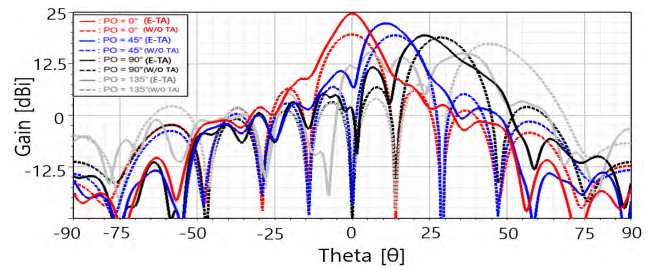
FIGURE 17. Simulated radiation patterns of the antenna with and without the proposed E-TA in YZ-plane at 28 GHz.
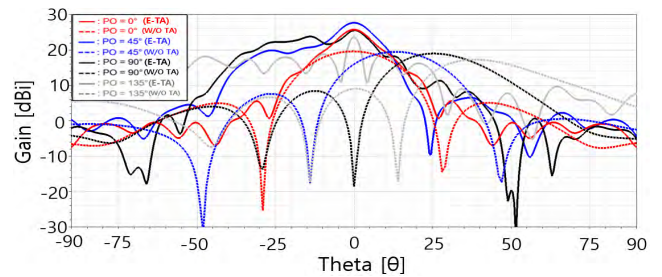
FIGURE 18. Simulated radiation patterns of the antenna with and without the proposed E-TA in XZ-plane at 28 GHz.

The peak gain of the antenna with the proposed transmit array is almost 4.5 dB higher than that of the antenna without the transmit array at boresight. The steered angles at which the peak gains are observable for the four POs are 0°, 11°, 23°, and 36°. Fig. 18 shows radiation patterns in XZ-plane of the antenna with and without E-TA. The solid lines and dashed lines are radiation patterns of the antenna with and without the proposed E-TA respectively. As shown in Fig. 17 and 18, when antenna beam is steered the E-TA suffers scan losses with distorted radiation patterns.

B. MACRO DESIGN OF FR4-BASED R-TA

As shown in Fig. 17, the E-TA causes a significant scan loss when antenna beam is steered since the E-TA is designed for boresight angle. As a compromise to provide wide coverage along one axis, this scan loss issue can be mitigated by applying phase compensation to only x-axis. Newly designed transmit array is shown in Fig. 19 where rectangular transmit array denoted by R-TA. Design steps are same as those of the E-TA and the size of the R-TA is 152 mm×152 mm. To achieve a reliable beam steering along y-axis, only Table 2 is applied along the x-axis but the unit cells having a same type are arranged along the y-axis. The R-TA has straight unit cell distribution along the beam steering axis to achieve gain enhancement in steering beam. The gain enhancement of the proposed R-TA relative to that of the patch array antenna for POs of 0°, −45°, −90°, and −135° in YZ-plane is observable in the full-wave EM simulation results in Fig. 20. The solid lines are the radiation patterns of the antenna with the proposed R-TA, and the dashed lines are the radiation patterns of the antenna without any transmit array. The peak gain
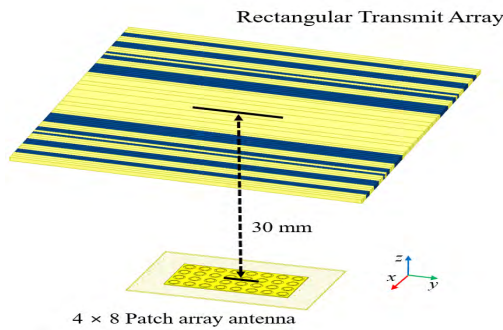
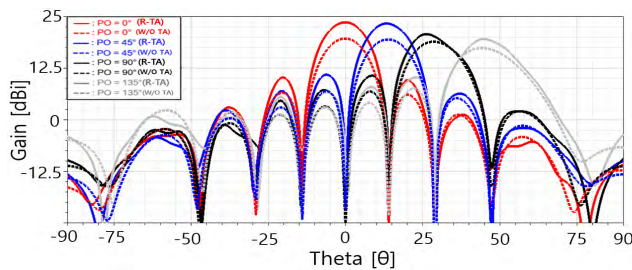**FIGURE 19.** Oblique perspective of the proposed effective medium-based R-TA fed by a 4 × 8 patch array antenna.

FIGURE 20. Simulated radiation patterns of the antenna with and without the proposed R-TA in YZ-plane at 28 GHz.
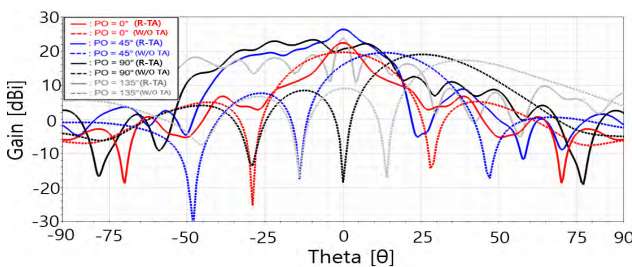

FIGURE 21. Simulated radiation patterns of the antenna with and without the proposed R-TA in XZ-plane at 28 GHz.

of the antenna with the proposed transmit array is almost 3 dB higher than that of the antenna without the transmit array at boresight. The steered angles at which the peak gains are observable for the four POs are 0°, 13°, 26°, and 44.5°. Fig. 21 shows radiation patterns in XZ-plane of the antenna with and without the R-TA. The solid and dashed lines are radiation patterns of the antenna with and without the proposed E-TA respectively. Comparisons in radiation patterns of the E-TA and the R-TA at 28GHz are shown in Fig. 22. Except for at boresight, the gains of the R-TA are higher than those of the E-TA.

C. MACRO DESIGN OF FR4-BASED SATA

It should be noted that at some specific angles, gain enhancement by the rectangular transmit array (R-TA) is degraded because of mutual couplings among radiating unit cell elements, which have been a known issue as scan
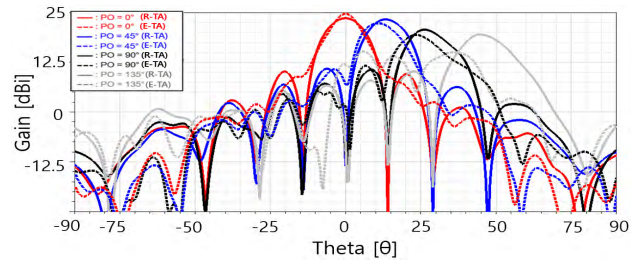

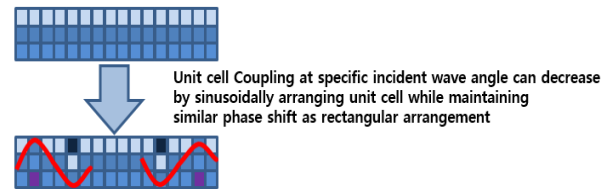**FIGURE 22.** Simulated radiation patterns of the E-TA and R-TA at 28GHz.

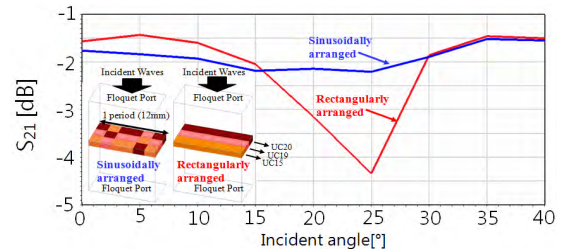**FIGURE 23.** Concept of spatially periodic arrangements of the unit cells.

FIGURE 24. A comparison of S_{21} between rectangularly and sinusodially arranged unit cells versus incident angle.

blindness [30]–[33]. This section addresses the mutual couplings resulting from the conventional unit cell placement rendering rectangular shapes and it is shown that this problem can be improved by utilizing the fact that radiating elements with spatially periodic arrangements can boost the antenna gain at specific angles shown in Fig. 23. Since the unit cell dimension is 2 mm and one period set consists of six unit cells, the lateral dimension of one period is 12 mm. Fig. 24 shows a comparison of S_{21} between the rectangularly and sinusoidally arranged unit cells versus incident angle. Red and blue lines are simulation results of the S_{21} of the rectangularly and sinusoidally arranged unit cells respectively. Utilization of the sinusoidally arranged unit cells decreases mutual coupling effect at the specific angle. But the S_{21} of the sinusoidally arranged unit cells is worse than that of the rectangularly arranged unit cells when incident angle changes 0° to 15°. As shown in Fig. 24 and 25, the radiation patterns of all-period case have gain degradation when phase offset is −45°.

Based on these heuristic study, 3 periods case is chosen to minimize scan loss at the desired coverage. Fig. 26 illustrates a new form of the proposed transmit array, a sinusoidally arranged transmit array (SATA) fed by a 4 × 8 patch array antenna. All of the design processes are same as those for the
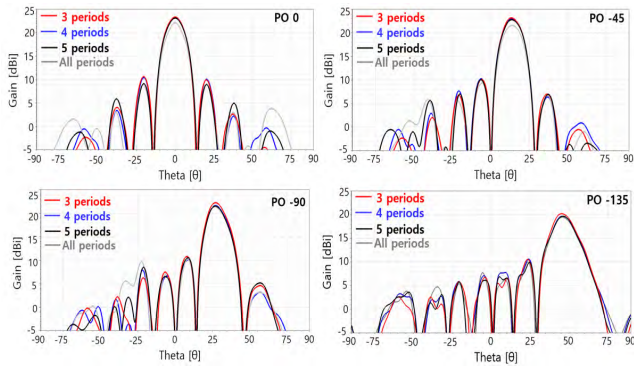
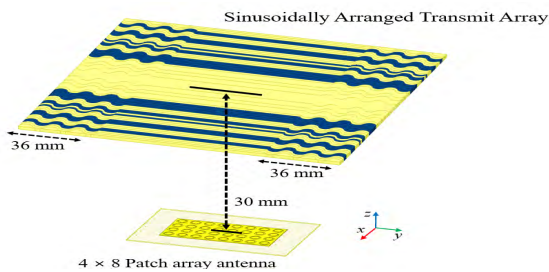**FIGURE 25. Comparisons of radiation patterns of TA consisting of sinusoidally arranged unit cells sets.**

FIGURE 26. Oblique view of the proposed effective medium-based SATA fed by a 4 × 8 patch array antenna.
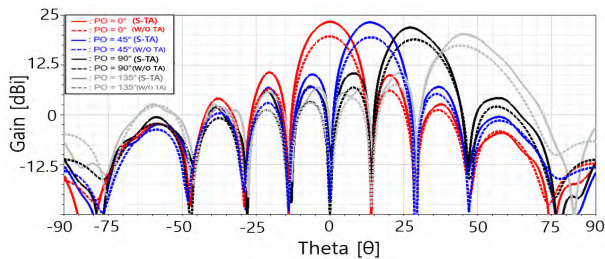

FIGURE 27. Simulated radiation patterns of the 4 × 8 antenna array with and without the proposed SATA, denoted as S-TA in YZ-plane at 28 GHz.

FIGURE 28. Simulated radiation patterns of the 4 × 8 antenna array with and without the proposed SATA, denoted as S-TA in XZ-plane at 28 GHz.
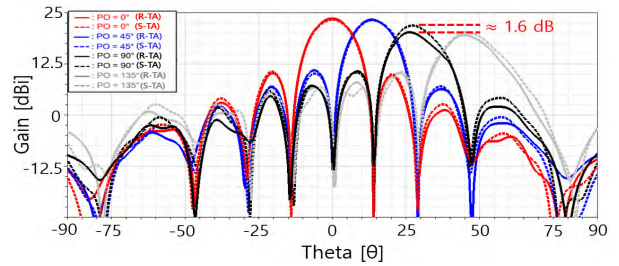
FIGURE 29. Simulated radiation patterns of the S-TA and R-TA at 28 GHz.
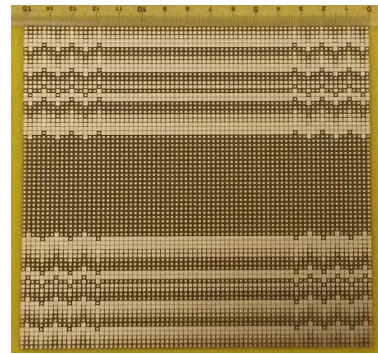
FIGURE 30. Top view of the fabricated SATA made of FR4 substrate.
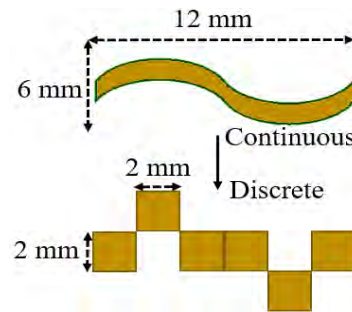
FIGURE 31. Disposition of the fabricated SATA unit cells in one period.

rectangularly-arranged FR4-based transmit array described in Section III-B except for the design of partially modified areas to have the sinusodially arranged unit cells. The rectangularly arranged unit cells in the initial design, were sinusoidally rearranged 36 mm inside the edge of R-TA.

The gain enhancement in YZ-plane of the SATA is shown in Fig. 27, compared to the 4 × 8 patch array antenna. The solid lines are the radiation patterns of the 4 × 8 patch array antenna combined with the proposed SATA, denoted as S-TA. The dashed lines are the radiation patterns of the antenna array without any transmit array. The peak gain of the SATA is 3 dB higher than that of the 4 × 8 patch array antenna at boresight. The steered angles of the SATA for the four POs are 0°, 13.5°, 26°, and 45°. Fig. 28 shows radiation patterns in XZ-plane of the antenna with and without SATA denoted by S-TA. The solid and dashed lines are radiation patterns of the antenna with and without the proposed S-TA respectively.

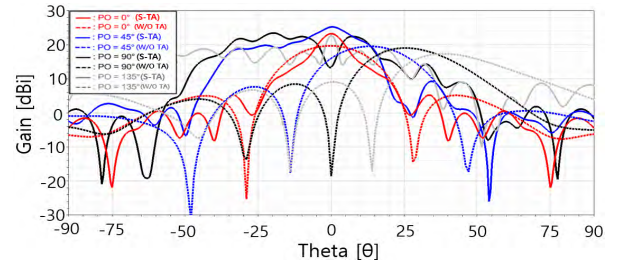Fig. 29 shows a radiation patterns comparison of S-TA and R-TA. Solid lines are radiation patterns of R-TA and dashed lines are radiation patterns of S-TA. Gain enhancement of S-TA is higher 1.6 dB than that of the R-TA at PO −90°.

D. FABRICATED SAMPLES AND MEASUREMENT
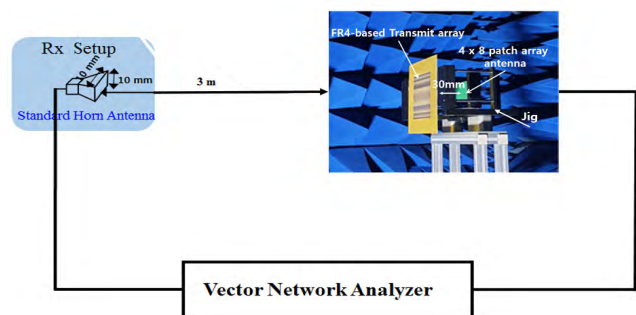
FIGURE 32. Measurement setup: 1. Tx setup consisting of a transmit array and a 4 × 8 patch array antenna (antenna source) and 2. Rx standard gain horn antenna.
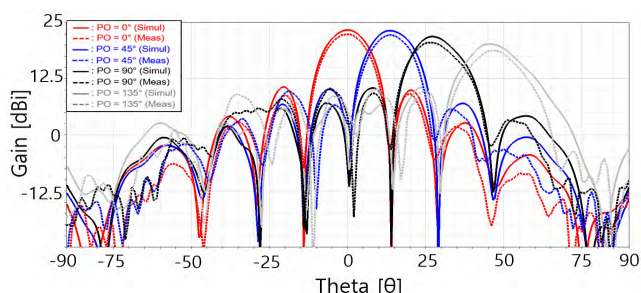
FIGURE 33. Simulated and measured radiation patterns of the antenna with the proposed SATA for four POs: 0°, −45°, −90°, and −135°.

OF SATA ANTENNA

A top view of the fabricated sample of FR4-based SATA is shown in Fig. 30. Ideally smooth shapes in the simulation model of the SATA are replaced by realizable discrete unit cells based on the effective medium-based SATA shown in Fig. 31. The entire thickness of the proposed transmit array is 1.04 mm, and two types of the dielectric materials, FR4 and Prepreg, are used. FR4 with a thickness of 0.2 mm is used as the substrate, and Prepreg with a thickness of 0.08 mm is used as the bonding layer between the adjacent FR4 substrates. Fig. 32 shows the measurement setup, where the proposed FR4-based SATA fed by the 4 × 8 patch array antenna serves as a transmitting (Tx) antenna and a standard gain horn antenna serves as a receiving (Rx) antenna. In the setup, the distance between 4 × 8 patch array antenna and transmit array measurement. In the setup, the distance between 4 × 8 patch array antenna and transmit array held by jig is 30 mm. The proposed transmit array is measured in anechoic chamber with a standard measurement setup. The holder is designed to support steering of the incident waves. The gain of the transmit array was extracted by measuring the received power before and after mounting the proposed FR4 transmit array in front of the 4 × 8 patch array antenna. The simulated and measured radiation patterns of the antenna with the SATA are shown in Fig. 33 for POs of 0°, −45°, −90°, and −135°. The steered angles at which the peak gains of the measured results occur for the four POs are 0°, 14°, 26°, and 44°. The overall

measured gains are in agreement with the simulated gains, with an error range of 0.8–1 dB.

V. CONCLUSION

A novel design approach enabling the fabrication of energy-efficient transmit arrays on FR4, a lossy substrate in the millimeter wave band, was presented in this paper. In this approach, the dielectric loss at a metal layer is interpreted as a parasitic resistance in a capacitance or an inductance in the equivalent circuit of the spatial filter. It was found that low-pass spatial filters are more vulnerable to lossy substrates than bandpass spatial filters because the E-fields of the inter-layers of low pass spatial filters are more coupled into other layers near them. Based on this information, mixed-order and disparate combinations of the spatial filters were designed appropriately for FR4-based transmit array design. It was confirmed that this approach can be used to produce affordable 28 GHz FR4-based transmit arrays. In addition, the 4 × 8 patch array antenna used in this study was briefly described. A novel technique of applying an effective medium structure in a transmit array simulation was demonstrated, and it was shown that the effective medium-based simulation is four times faster than FR4-based simulation and well represents FR4-based transmit arrays. This technique is promising for massive transmit array design and simulation.

Furthermore, several types of the transmit arrays were introduced: an E-TA, R-TA and a SATA. It was demonstrated that the 4 × 8 patch array antenna gain can be improved by employing an FR4-based transmit array, while the steered angle of an antenna with an FR4-based transmit array is almost same as that of an antenna without an FR4-based transmit array. This finding confirms that the scan loss is close to zero when the beam is steered along the axis where eight antenna elements are aligned. In addition, the overall measured gains were in agreement with the simulated gains, with an error range of 0.8 to 1 dB. Finally, it was confirmed that the proposed SATA can achieve gain enhancement at target steered angles. The proposed design approaches are promising for 5G outdoor customer premise equipment and repeaters where the conventional designs, fabrication conditions and material costs are highly limited due to complex and lossy characteristics.

REFERENCES
[1] N. Ojaroudiparchin, M. Shen, and G. F. Pedersen, "8 × 8 planar phased array antenna with high efficiency and insensitivity properties for 5G mobile base stations," in *Proc. 10th Eur. Conf. Antennas Propag.*, Davos, Switzerland, Apr. 2016, pp. 1–5.

[2] B. Thors, A. Furuskär, D. Colombi, and C. Törnevik, "Time-averaged realistic maximum power levels for the assessment of radio frequency exposure for 5G radio base stations using massive MIMO," *IEEE Access*, vol. 5, pp. 19711–19719, 2017.

[3] S. Hamid, M. T. Ali, Y. Yamada, N. H. Abd Rahman, and N. Michishita, "Application of negative index lens antenna for 5G mobile base station," in *Proc. Int. Symp. Antennas Propag. (ISAP)*, Busan, South Korea, Oct. 2018, pp. 1–2.

[4] K. R. Mahmoud and A. M. Montaser, "Performance of tri-band multi-polarized array antenna for 5G mobile base station adopting polarization and directivity control," *IEEE Access*, vol. 6., pp. 8682–8694, 2018.

[5] H. Lee, J. Bang, S. Lee, and J. Choi, "Phased array antenna with whole-metal-cover for mm-Wave 5G mobile phone applications," in *Proc. IEEE Int. Workshop Electromagn., Appl. Student Innov. Competition (iWEM)*, Nagoya, Japan, Aug. 2018, p. 1.

[6] K. Zhao, Z. Ying, and S. He, "EMF exposure study concerning mmWave phased array in mobile devices for 5G communication," *IEEE Antennas Wireless Propag. Lett.*, vol. 15, pp. 1132–1135, 2016.

[7] E. Park, Y. J. Yoon, and H. Kim, "dual polarization L-shaped slot array antenna for 5G metal-rimmed mobile phone," in *Proc. Int. Symp. Antennas Propag. (ISAP)*, Busan, South Korea, Oct. 2018, pp. 1–2.

[8] *5G Outdoor CPE Test Report*. Accessed: Jun. 10, 2019. [Online]. Available: https://fccid.io/A3LSFG-D1100/Test-Report/mmWave-Test-Report-3780718

[9] B. Rahmati and H. R. Hassani, "Low-profile slot transmitarray antenna," *IEEE Trans. Antennas Propag.*, vol. 63, no. 1, pp. 174–181, Jan. 2015.

[10] N. Behdad, M. Al-Joumayly, and M. Salehi, "A low-profile third-order bandpass frequency selective surface," *IEEE Trans. Antennas Propag.*, vol. 57, no. 2, pp. 460–466, Feb. 2009.

[11] M. A. Al-Joumayly and N. Behdad, "Wideband planar microwave lenses using sub-wavelength spatial phase shifters," *IEEE Trans. Antennas Propag.*, vol. 59, no. 12, pp. 4542–4552, Dec. 2011.

[12] M. Li and N. Behdad, "Frequency selective surfaces for pulsed high-power microwave applications," *IEEE Trans. Antennas Propag.*, vol. 61, no. 2, pp. 677–687, Feb. 2013.

[13] C. Pfeiffer and A. Grbic, "Millimeter-wave transmitarrays for wavefront and polarization control," *IEEE Trans. Microw. Theory Techn.*, vol. 61, no. 12, pp. 4407–4417, Dec. 2013.

[14] J. Oh, "Millimeter-wave thin lens employing mixed-order elliptic filter arrays," *IEEE Trans. Antennas Propag.*, vol. 64, no. 7, pp. 3222–3227, Jul. 2016.

[15] K. Pham, N. T. Nguyen, A. Clemente, L. Di Palma, L. Le Coq Laurent Dussopt, and R. Sauleau, "Design of wideband dual linearly polarized transmitarray antennas," *IEEE Trans. Antennas Propag.*, vol. 64, no. 5, pp. 2022–2026, May 2016.

[16] K. K. Katarea, A. Biswas, and M. J. Akhtar, "Microwave beam steering of planar antennas by hybrid phase gradient metasurface structure under spherical wave illumination," *J. Appl. Phys.*, vol. 122, no. 23, 2017, Art. no. 234901.

[17] A. R. Weily, K. P. Esselle, B. C. Sanders, and T. S. Bird, "High-gain 1D EBG resonator antenna," *Microw. Opt. Technol. Lett.*, vol. 47, no. 2, pp. 107–114, Oct. 2005.

[18] Y. Ge, K. P. Esselle, and Y. Hao, "Design of low-profile high-gain EBG resonator antennas using a genetic algorithm," *IEEE Antennas Wireless Propag. Lett.*, vol. 6, pp. 480–483, 2007.

[19] B. A. Zeb, Y. Ge, K. P. Esselle, Z. Sun, and M. E. Tobar, "A simple dual-band electromagnetic band gap resonator antenna based on inverted reflection phase gradient," *IEEE Trans. Microw. Theory Techn.*, vol. 60, no. 10, pp. 4522–4528, Oct. 2012.

[20] X. Y. Jiang, *Metamaterials: Theory, Design, and Applications*. Rijeka, Croatia: InTech, 2012.

[21] M. A. Al-Joumayly and N. Behdad, "A generalized method for synthesizing low-profile, band-pass frequency selective surfaces with non-resonant constituting elements," *IEEE Trans. Antennas Propag.*, vol. 58, no. 12, pp. 4033–4041, Dec. 2010.

[22] M. Li and N. Behdad, "Wideband true-time-delay microwave lenses based on metallo-dielectric and all-dielectric lowpass frequency selective surfaces," *IEEE Trans. Antennas Propag.*, vol. 61, no. 8, pp. 4109–4119, Aug. 2013.

[23] J. Oh, "Millimeter-wave short-focus thin lens employing disparate filter arrays," *IEEE Antennas Wireless Propag. Lett.*, vol. 15, pp. 1446–1449, 2016.

[24] G. Shaker, "Electromagnetic band gap structures: Design and application in antenna systems," M.S. thesis, Dept. Elect. Comput. Eng., Univ. Waterloo, Waterloo, ON, USA, 2006.

[25] K. Sarabandi and N. Behdad, "A frequency selective surface with miniaturized elements," *IEEE Trans. Antennas Propag.*, vol. 55, no. 5, pp. 1239–1245, May 2007.

[26] W. Hong, S.-T. Ko, Y. Lee, and K.-H. Baek, "Compact 28 GHz antenna array with full polarization flexibility under yaw, pitch, roll motions," in *Proc. 9th Eur. Conf. Antennas Propag. (EuCAP)*, Lisbon, Portugal, Apr. 2015, pp. 1–3.

[27] W. Hong, S.-T. Ko, Y. Lee, and K.-H. Baek, "Multi-polarized antenna array configuration for mmWave 5G mobile terminals," in *Proc. Int. Workshop Antenna Technol. (iWAT)*, Seoul, South Korea, Mar. 2015, pp. 60–61.

[28] G. S. Karthikeya, M. P. Abegaonkar, and S. K. Koul, "Low cost high gain triple band mmWave Sierpinski antenna loaded with uniplanar EBG for 5G applications," in *Proc. IEEE Int. Conf. Antenna Innov. Mod. Technol. Ground, Aircr. Satell. Appl. (iAIM)*, Bangalore, India, Nov. 2017, pp. 1–5.

[29] I. Yoon and J. Oh, "Millimeter-wave thin lens using multi-patch incorporated unit cells for polarization-dependent beam shaping," *IEEE Access*, vol. 7, pp. 45504–45511, 2019.

[30] D. Pozar and D. Schaubert, "Scan blindness in infinite phased arrays of printed dipoles," *IEEE Trans. Antennas Propag.*, vol. 32, no. 6, pp. 602–610, Jun. 1984.

[31] O. I. Yastrebtsova, "Surface waves and effect of scan blindness in microstrip antenna array," (in Russian), *Fundanentalnye Problemyraio-electronnogo Priborostroeniya, Moscow*, vol. 4, pp. 1035–1038, 2017.

[32] B. Avser and V. B. Erturk, "A new method for the prognosis of scan blindness angle in finite phased arrays of printed dipoles," in *Proc. 5th Eur. Conf. Antennas Propag. (EUCAP)*, Apr. 2011, pp. 1014–1017.

[33] N. Amitay, V. Galindo, and C. P. Wu, *Theory and Analysis of Phased Array Antennas*. New York, NY, USA: Wiley, 1972.

YONGYEON KIM (S'17) received the B.S and M.S degrees from Inha University, South Korea, in 2015 and 2017, respectively. In 2017, he was a Research Engineer with the Millimeter Multi-scale Wave Laboratory, Inha University, working on the development of an RF design program for basic RF circuit design and education. He is currently a Hardware Research Engineer with KMW Corporation, working on the development of a massive MIMO antenna for 5G communication below 6 GHz. He also participates in antenna weight factor optimization for low scan loss, enabling 5G NR beamforming. His current research interests include massive MIMO antenna design, millimeter-wave beam focusing/shaping techniques, and hybrid beamforming for massive MIMO systems.

HOGYEOM KIM received the B.S degree from Inha University, South Korea, in 2016, where he was a Research Engineer with the Millimeter Multiscale Wave Laboratory. He is currently pursuing the M.S. degree with Seoul National University, South Korea.

His current research interests include transmit array antennas for 5G communication and millimeter-wave radar systems.

INSEOP YOON received the B.S. degree in electronics engineering from Korea Polytechnic University, South Korea, in 2011, and the M.S. degree in electronics engineering from Inha University, South Korea, in 2013, where he is currently pursuing the Ph.D. degree. His current research interests include antenna design for 5G telecommunication and millimeter-wave radar systems.

JUNGSUEK OH (SM'17) received the B.S. and M.S. degrees from Seoul National University, South Korea, in 2002 and 2007, respectively, and the Ph.D. degree from the University of Michigan at Ann Arbor, in 2012.

From 2007 to 2008, he was a Hardware Research Engineer with Korea Telecom, working on the development of flexible RF devices. In 2012, he was a Postdoctoral Research Fellow with the Radiation Laboratory, University of Michigan. From 2013 to 2014, he was a Staff RF Engineer with Samsung Research America, Dallas, working as the Project Leader for the 5G/millimeter-wave antenna system. From 2015 to 2018, he was a Faculty Member with the Department of Electronic Engineering, Inha University, South Korea. He is currently an Assistant Professor with the Department of Electrical and Computer Engineering, Seoul National University, South Korea. He has published more than 40 technical journals and conference papers. His research interests include millimeter-wave beam focusing/shaping techniques, antenna miniaturization for integrated systems, and radio propagation modeling for indoor scenarios. He has served as a TPC Member and as the Session Chair for the IEEE AP-S/USNC-URSI and ISAP. He was a recipient of the 2011 Rackham Predoctoral Fellowship Award at the University of Michigan. He has served as a Technical Reviewer for the IEEE Transactions on Antennas and Propagation and the IEEE Antenna and Wireless Propagation Letters, among other journals.

• • •